Role of diffusion in crystallization of hard-sphere colloids

Michael A. Lam [1,*] Boris Khusid [1,†] Lou Kondic [1,‡] and William V. Meyer [2,§]
[1]*New Jersey Institute of Technology, Newark, New Jersey 07102, USA*
[2]*Universities Space Research Association at NASA Glenn Research Center, Cleveland, Ohio 44135, USA*

(Received 21 August 2021; accepted 12 October 2021; published 12 November 2021)

Vital for a variety of industries, colloids also serve as an excellent model to probe phase transitions at the individual particle level. Despite extensive studies, origins of the glass transition in hard-sphere colloids discovered about 30 y ago remain elusive. Results of our numerical simulations and asymptotic analysis suggest that cessation of long-time particle diffusivity does not suppress crystallization of a metastable liquid-phase hard-sphere colloid. Once a crystallite forms, its growth is then controlled by the particle diffusion in the depletion zone surrounding the crystallite. Using simulations, we evaluate the solid-liquid interface mobility from data on colloidal crystallization in terrestrial and microgravity experiments and demonstrate that there is no drastic difference between the respective mobility values. The insight into the effect of vanishing particle mobility and particle sedimentation on crystallization of colloids will help engineer colloidal materials with controllable structure.

DOI: 10.1103/PhysRevE.104.054607

I. INTRODUCTION

Understanding the dynamics of phase transitions at the individual particle level is a long-standing challenge in physics. Colloids serve as an excellent model for direct real-space observation of these phenomena at the individual particle level [1–5]. In addition, colloids are vital for a variety of industries, from 3D printing to photonics and electronics and to chemicals and pharmaceuticals. However, our current understanding of microstructural evolution and phase transformation in colloids is still elusive. The following findings on hard-sphere colloids illustrate this point.

Molecular-dynamics simulations predict that the phase behavior of hard spheres, the simplest model of matter with a crystallization transition, is solely determined by the particle volume fraction [1–5]: a liquid phase for particle volume fraction φ up to the freezing point $\varphi_{\rm fr} \approx 0.49$, a crystalline phase for φ from the melting point $\varphi_{\rm m} \approx 0.54$ up to $\varphi_0 = \sqrt{2}\pi/6 \approx 0.74$, and coexisting liquid and crystalline phases for $\varphi_{\rm fr} < \varphi < \varphi_{\rm m}$. These freezing and melting points are well reproduced by experiments on model colloids like dispersions of micrometer-sized sterically stabilized polymethylmethacrylate (PMMA) particles in hydrocarbon solvents [1–5]. Unexpectedly, seminal experiments by Pusey and van Megen in the mid-1980s [6,7] revealed that homogeneous crystallization of a monodisperse suspension for $\varphi > 0.57-0.58$ did not occur for months. The point $\varphi_{\rm g} \approx 0.57-0.58$ was identified as the glass transition and attributed to the cessation of the particle long-time diffusion. However, the glassy structure was not observed in large-scale molecular-dynamics simulations of hard spheres [8,9]. Surprisingly, experiments in the Space Shuttle in 1995 and 1998 revealed that shear-melted hard-sphere suspensions with $\varphi \sim 0.59-0.63 > \varphi_{\rm g}$ crystallized in microgravity within several days [10,11]. These samples survived reentry and remained crystalline on Earth. But, once shear melted on Earth, they did not crystallize again [10,11]. Despite extensive studies, origins of the glass transition in colloidal suspensions routinely observed in terrestrial experiments but not in microgravity remain unexplained [12–19].

The main goal of the presented numerical simulations and asymptotic analysis is to demonstrate that cessation of the particle long-time diffusion does not arrest crystallization of a metastable liquid-phase hard-sphere colloid. We then use numerical simulations to evaluate the solid-liquid interface mobility from the data on colloidal crystallization in terrestrial and microgravity experiments. It is found that there is no drastic difference between their values. Summarizing the known information about colloidal crystallization in terrestrial and microgravity experiments allows us to suggest that gravitational sedimentation of particles within the diffusion zone around a crystallite hinders crystallization of colloids when the particle volume fraction is greater than $\varphi_{\rm g} \sim 0.57-0.58$.

II. MODEL FORMULATION

Experiments reveal that homogeneous crystallization of hard-sphere colloids can be divided into four stages [20–24]. The first (*induction*), involves formation of crystal precursors containing a few hundred to a few thousand particles. While displaying some features of the orientational order, they do not show long-range translational order. The crystalline periodicity appears in the second stage (*conversion*) during which the precursors convert into true crystallites and begin to grow. The

*mal37@njit.edu
†khusid@njit.edu
‡kondic@njit.edu
§william.v.meyer@nasa.gov

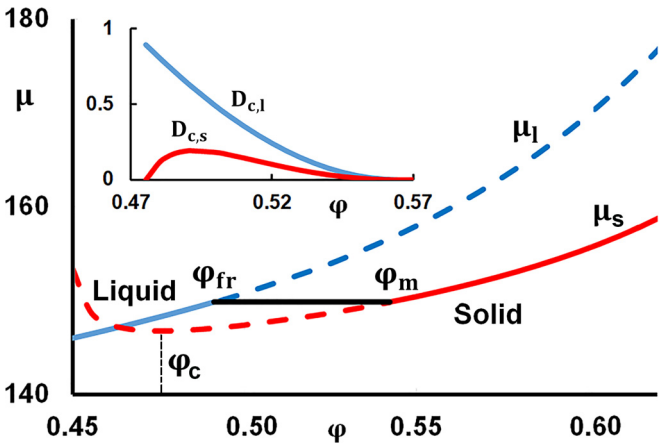

FIG. 1. Particle chemical potential in units k_BT in the liquid μ_l and μ_s solid phase vs volume fraction φ in this phase; solid and dashed curves show stable and metastable branches. Inset (see text) shows $D_{c,l}$, $D_{c,s}$ in units D_0 vs volume fraction φ.

gap between the formation and conversion of precursors into crystallites tends to disappear in dense suspensions which are in the fully crystalline state above the melting point [22]. The number of crystallites and the sample crystallinity show their strongest increase in the third stage (*main crystallization*). In the fourth (*ripening*), coarsening dominates as larger crystals grow while the smaller ones disappear.

We consider the second and third stages of crystallization of hard-sphere colloids where the particle diffusion transport plays the major role. The diffusion mechanism of the crystallite growth in hard-sphere colloids is confirmed by observation of a thin depletion zone surrounding a growing crystallite. It was first recorded in Refs. [25,26] and later confirmed in other experiments (see reviews in Refs. [1,4,5,27–30]). Modeling of diffusion processes accompanied by a liquid-solid transition requires equations for the chemical potentials and diffusion transport of colloidal particles in the liquid and solid phases. We use results of molecular-dynamics (MD) simulations of hard spheres [31,32] to express the chemical potential, $k_BT\mu_l(\varphi_l)$ and $k_BT\mu_s(\varphi_s)$, and the osmotic pressure, $k_BT\Pi_l(\varphi_l)/V_p$ and the $k_BT\Pi_s(\varphi_s)/V_p$, in the liquid and solid phases as a function of the volume fraction in the colloid, φ_l and φ_s ($> \varphi_c = 0.475$) (Fig. 1); here V_p is the particle volume, k_B and T are the Boltzmann constant and absolute temperature, liquid and solid phases are, respectively, denoted by a subscript l and s, and $d\mu_s/d\varphi_s = 0$ at $\varphi_s = \varphi_c$. Equations of Refs. [31,32] were recently confirmed [33].

The nondimensional chemical potential, $\mu_{l,s}$, and osmotic pressure, $\Pi_{l,s}$, in the colloid liquid and solid phases, respectively denoted by a subscript l and s, are expressed in terms of the compressibility factor $Z_{l,s}(\varphi)$ computed in Refs. [31,32]:

$$\begin{aligned}\mu_{l,s}(\varphi_{l,s}) &= \int \frac{Z_{l,s}(\varphi_{l,s})}{\varphi_{l,s}} d\varphi_{l,s} + Z_{l,s}(\varphi_{l,s}) + c_{l,s},\\ \Pi_{l,s}(\varphi_{l,s}) &= \varphi_{l,s} Z_{l,s}(\varphi_{l,s}),\\ \frac{d\mu_{l,s}}{d\varphi_{l,s}} &= \frac{1}{\varphi_{l,s}} \frac{d\Pi_{l,s}}{d\varphi_{l,s}},\end{aligned} \tag{1}$$

where the indices l and s denote the liquid and solid phase and $c_{l,s}$ are some constants of integration. The liquid phase $Z_l(\varphi_l)$ with its two derivatives are continuous at φ_{fr}; $Z_s(\varphi_s)$ is taken for the hexagonal close-packed crystal [32]; alternatively face-centered cubic could be used here. However, the difference of about 0.2% between coefficients for compressibility factors of these two phases is not so significant to modify considerably the presented results. We note that $Z_s(\varphi_s)$ has singular points at the maximum volume fraction φ_0 and at $\varphi_c = 0.4753$, where $d\mu_s/d\varphi_s = 0$ [32]. As the chemical potentials at the freezing and melting points are equal, we find $c_s - c_l = 135.7439$.

We consider the initial formation of crystallites when diffusion zones around different crystallites do not overlap and each crystallite grows independently. Similar in spirit to Refs. [27–29], we use the classical model for the crystallite growth that combines diffusion equations for the particle transport in the liquid and solid phases coupled with the particle flux balance and thermodynamic relations at the crystallite surface. We use the classical Wilson-Frenkel law [34,35] to model the motion of the solid-liquid interface as it was well confirmed by experiments on various colloids [3,4,28]. In this case, the model for the growth of a spherical crystallite in a metastable liquid-phase suspension with the particle volume fraction φ_{out} combines the diffusion equations for the volume fraction of particles in the liquid φ_l and solid φ_s phases:

$$\frac{\partial \varphi_l}{\partial t} = \frac{1}{r^2}\frac{\partial}{\partial r}\left[r^2 D_{c,l}(\varphi_l)\frac{\partial \varphi_l}{\partial r}\right] \quad \text{for } R(t) \leqslant r$$
$$\text{with } \varphi_l \to \varphi_{out} \text{ at } r \to \infty, \tag{2}$$

$$\frac{\partial \varphi_s}{\partial t} = \frac{1}{r^2}\frac{\partial}{\partial r}\left[r^2 D_{c,s}(\varphi_s)\frac{\partial \varphi_s}{\partial r}\right] \quad \text{for } 0 \leqslant r \leqslant R(t)$$
$$\text{with } \frac{\partial \varphi_s}{\partial r} \to 0 \text{ and } r \to 0 \tag{3}$$

In these equations, the spatial coordinate r and the crystallite radius R are scaled by the particle radius a and the time by a^2/D_0, where $D_0 = k_BT/6\pi\eta_f a$ is the Stokes-Einstein diffusion coefficient of a sphere in the solvent with viscosity η_f at absolute temperature T; k_B is the Boltzmann constant; $D_{c,l}$ and $D_{c,s}$ are the collective (or mutual) diffusion coefficients of particles in the liquid and solid phases, respectively.

Following irreversible thermodynamics (e.g., Ref. [36]), the collective (or mutual) diffusion coefficients in the liquid and solid phases are $D_0D_{c,l}$ and $D_0D_{c,s}$ (inset in Fig. 1), respectively, where

$$\begin{aligned}&D_{c,l} = M_L(\varphi_l)d\mu_l/d\varphi_l, \quad D_{c,s} = M_L(\varphi_s)d\mu_s/d\varphi_s\\ &M_L = (1-\varphi_l/\varphi_g)^{\zeta_L}, \quad M_s = (1-\varphi_l/\varphi_b)^{\zeta_S}.\end{aligned} \tag{4}$$

The power-law expressions for concentration dependence of the particle long-time self-diffusivity, M_L with $\varphi_g = 0.57$, $\zeta_L = 2.6$, and short-time self-diffusivity, M_s with $\varphi_b = 0.72$, $\zeta_S = 1.56$, in the liquid phase are taken from Refs. [37,38]. A power law for concentration dependence of the self-diffusivity with the very similar coefficients was also extracted from MD simulations [17]. The same dependence is used in Eq. (4) for the solid phase as there exist no measurements. Ratios M_L/M_s equal to 0.051 at $\varphi_s = \varphi_c$ and 0.035 at $\varphi_l = \varphi_{fr}$ are consistent,

although smaller, with the value 0.098 proposed for the so-called dynamic freezing transition; see Refs. [39,40].

The boundary conditions for Eqs. (2) and (3) at the moving solid-liquid interface R(t) include the particle flux balance, where φ_{sR} and φ_{lR} are, respectively, the particle volume fractions at the solid and liquid sides of the interface

$$(\varphi_{sR}-\varphi_{lR})\frac{dR}{dt}=D_{c,l}(\varphi_{lR})\frac{\partial\varphi_l}{\partial r}\bigg|_{r=R}-D_{c,s}(\varphi_{sR})\frac{\partial\varphi_s}{\partial r}\bigg|_{r=R}, \tag{5}$$

the pressure balance at the crystallite surface

$$\Pi_s(\varphi_{sR})=\Pi_l(\varphi_{lR})+\Gamma/R, \tag{6}$$

and the Wilson-Frenkel law for the velocity of the solid-liquid interface scaled as $D_0 v_R/a$:

$$\frac{dR}{dt}=v_R \quad \text{with} \quad v_R=v_\infty J \quad \text{with} \quad J=1-e^F,$$
$$F=\mu_s(\varphi_{sR})-\mu_l(\varphi_{lR})+\Gamma/(\varphi_{sR}R) \tag{7}$$

Here the surface tension averaged over all interface orientations is taken as $3\Gamma k_B T/8\pi a^2$ with $\Gamma=0.15$ [24], F is a change in the Gibbs energy per particle in units of k_BT when it jumps from the liquid to the solid side of the interface, and v_∞ is referred to as the solid-liquid interface mobility (or kinetic prefactor).

The appearance of the exponential factor J in Eq. (7) is captured by molecular-dynamics simulations which, however, do not provide reliable data on v_∞ due to a small number of particles used. The Wilson-Frenkel law considers that the transient ordering of particles at the solid-liquid interface is governed by the translational diffusion of particles in the supercooled liquid. It is currently hypothesized [3–5,27–29] that $v_\infty=\alpha m(\varphi_{lR})/2$, where $\alpha/2$ accounts for a difference in the particle diffusivity in the transition region between the solid and liquid phases and in the bulk liquid, and m stands for either the particle long-time, M_L, or short-time, M_s, diffusivity in the bulk liquid. We note that α is the only free parameter in our model. Previous theories [27–29] ignore the strong concentration dependence of the particle transport by taking $D_{c,l}$ and $D_{c,s}$ as the constants in Eqs. (2) and (3) and simplified Eqs. (6) and (7) by ignoring variations in the composition of the solid-liquid interface. A conservative finite-volume method with an adaptive mesh used to solve Eqs. (2)–(7) is described in the Appendix.

The crucial feature of our formulation is that we include the facts that (i) increasing the volume fraction reduces and eventually arrests the particle diffusion, and (ii) the composition of a growing crystallite changes with size. Previous approaches sidestepped these major features of colloids.

A. Crystallite dynamics

Equations (6) and (7) specify the interface volume fraction of the liquid φ_{lR} and solid φ_{sR} phases as a function of the crystallite size R and F. A general requirement for mechanical stability of the suspension liquid and solid phases implies that their osmotic pressure and the compressibility factor in Eq. (1) should increase monotonically with the particle volume fraction: $d\Pi_l/d\varphi_{lR}>0$, $d\Pi_s/d\varphi_{sR}>0$, $dZ_s/d\varphi_{sR}>0$.

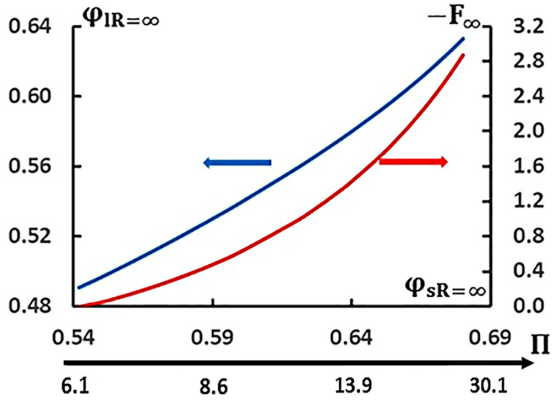

FIG. 2. Values of $\varphi_{lR=\infty}$, $\varphi_{sR=\infty}$ and $-F_\infty=\mu_l(\varphi_{lR=\infty})-\mu_s(\varphi_{sR=\infty})$ computed from Eqs. (8) for the flat interface, $1/R=0$, are shown vs the nondimensional osmotic pressure $\Pi=\Pi_l(\varphi_{lR=\infty})-\Pi_s(\varphi_{sR=\infty})$.

To examine the variation of φ_{lR} and φ_{sR} in the plane of R and F, we begin with a flat solid-liquid interface when $1/R=0$. The asymptotic solution of Eqs. (6) and (7) for a sufficiently large R can be presented as

$$\varphi_{lR}\approx\varphi_{lR=\infty}+a_{l\infty}/R,$$
$$\varphi_{sR}\approx\varphi_{sR=\infty}+a_{s\infty}/R, \quad \text{and}$$
$$F\approx F_\infty+f_\infty/R,$$

where $\varphi_{lR=\infty}$ and $\varphi_{sR=\infty}$ are given by the following equations for a flat solid-liquid interface:

$$\Pi_s(\varphi_{sR=\infty})=\Pi_l(\varphi_{lR=\infty}) \text{ and } F_\infty=\mu_s(\varphi_{sR=\infty})-\mu_l(\varphi_{lR=\infty}), \tag{8}$$

with $a_{l\infty}$, $a_{s\infty}$, and f_∞ related to one another as

$$a_{s\infty}\frac{d\Pi_s}{d\varphi_{sR}}\bigg|_{\varphi_{sR=\infty}}=a_{l\infty}\frac{d\Pi_l}{d\varphi_{lR}}\bigg|_{\varphi_{lR=\infty}}+\Gamma \quad \text{and}$$
$$f_\infty=\frac{a_{s\infty}}{\varphi_{sR=\infty}}\frac{d\Pi_s}{d\varphi_{sR}}\bigg|_{\varphi_{sR=\infty}}-\frac{a_{l\infty}}{\varphi_{lR=\infty}}\frac{d\Pi_l}{d\varphi_{lR}}\bigg|_{\varphi_{lR=\infty}}+\frac{\Gamma}{\varphi_{sR=\infty}}.$$

The values $\varphi_{lR=\infty}$, $\varphi_{sR=\infty}$, and F_∞ computed for the flat interface, $1/R=0$, are shown in Fig. 2.

The equilibrium $F_\infty=0$ represents the melting and freezing points $\varphi_{sR=\infty}=\varphi_m$ and $\varphi_{lR=\infty}=\varphi_{fr}$. Since the osmotic pressure in both suspension phases rises monotonically with the particle volume fraction and $\Pi_l(\varphi_{fr})=\Pi_s(\varphi_m)$, there exist only two cases: $\varphi_{sR=\infty}<\varphi_m$ and $\varphi_{lR=\infty}<\varphi_{fr}$ or $\varphi_{sR=\infty}>\varphi_m$ and $\varphi_{lR=\infty}>\varphi_{fr}$. The derivatives of F_∞ with respect to $\varphi_{lR=\infty}$ and $\varphi_{sR=\infty}$ are negative as $\varphi_{lR\infty}<\varphi_{sR\infty}$ while the derivative $d\varphi_{lR\infty}/d\varphi_{sR\infty}$ is positive:

$$\frac{dF_\infty}{d\varphi_{lR\infty}}=-\left(\frac{1}{\varphi_{lR\infty}}-\frac{1}{\varphi_{sR\infty}}\right)\frac{d\Pi_l}{d\varphi_{lR\infty}},$$
$$\frac{dF_\infty}{d\varphi_{sR\infty}}=-\left(\frac{1}{\varphi_{lR\infty}}-\frac{1}{\varphi_{sR\infty}}\right)\frac{d\Pi_s}{d\varphi_{sR\infty}} \quad \text{and}$$
$$\frac{d\Pi_l}{d\varphi_{lR\infty}}\frac{d\varphi_{lR\infty}}{d\varphi_{sR\infty}}=\frac{d\Pi_s}{d\varphi_{sR\infty}}$$

Accordingly, a flat crystallite would be stable for $\varphi_{lR=\infty} = \varphi_{fr}$, $\varphi_{sR=\infty} = \varphi_m$ when $F_\infty = 0$; would grow for $\varphi_{sR=\infty} > \varphi_m$, $\varphi_{lR=\infty} > \varphi_{fr}$ when $F_\infty < 0$; and would melt for $\varphi_{sR=\infty} < \varphi_m$, $\varphi_{lR=\infty} < \varphi_{fr}$ when $F_\infty > 0$.

We now consider the variation of φ_{lR} and φ_{sR} in the plane of R and F. For $F = 0$, they define the radius of a critical crystallite R_{cr} as a function of its composition $\varphi_{sR_{cr}}$ and the composition of the surrounding liquid $\varphi_{lR_{cr}}$. For a fixed value of φ_{lR} equal to $\varphi_{lR=\infty}$, Eqs. (6) and (7) provide φ_{sR} and F as functions of R and $\varphi_{lR=\infty}$. The derivatives of φ_{sR} and F with respect to R are

$$\frac{d\Pi_s}{d\varphi_{sR}}\frac{\partial\varphi_{sR}}{\partial R} = -\frac{\Gamma}{R^2} < 0 \quad \text{and}$$

$$\frac{\partial F}{\partial\varphi_{sR}} = \frac{1}{\varphi_{sR}^2}\left(\Pi_l + \Pi_s + 2\varphi_{sR}^2\frac{dZ_s}{d\varphi_{sR}}\right) > 0.$$

With R decreasing, magnitudes of φ_{sR} and F monotonically rise along the curve in the plane of R and F from their values $\varphi_{sR\infty}$ and F_∞ at $R \to \infty$. The variation of the sign of F along this curve depends on the sign of its value F_∞ which is determined by $\varphi_{lR=\infty}$ or $\varphi_{sR=\infty}$. As F_∞ is positive for $\varphi_{lR=\infty} < \varphi_{fr}$, F remains positive along the entire curve. Therefore, crystallites would melt in the liquid of the composition $\varphi_{lR=\infty}$ if their composition and size lie on this curve. As F_∞ is negative for $\varphi_{lR=\infty} > \varphi_{fr}$, F increases remaining negative for R greater than R_{cr}, crosses zero at the value of R_{cr}, and then remains positive for $R < R_{cr}$. Thus, crystallites whose composition and size lie on this curve would melt in the metastable liquid of the composition $\varphi_{lR=\infty}$ for $R < R_{cr}$ and grow for $R > R_{cr}$; φ_{sR} is accordingly greater than $\varphi_{sR_{cr}}$ for the former and smaller for the latter.

Similarly, Eqs. (6) and (7) provide φ_{lR} and F as functions of R for a fixed value of φ_{sR} equal to $\varphi_{sR=\infty}$. The derivatives of φ_{lR} and F with respect to R are

$$\frac{d\Pi_l}{d\varphi_{lR}}\frac{\partial\varphi_{lR}}{\partial R} = \frac{\Gamma}{R^2} > 0 \quad \text{and}$$

$$\frac{\partial F}{\partial\varphi_{lR}} = -\left(\frac{1}{\varphi_{lR}} + \frac{1}{\varphi_{sR}}\right)\frac{d\Pi_l}{d\varphi_{lR}} < 0.$$

The presented analysis demonstrates that crystallites of any size would melt in the stable liquid-phase composition of $\varphi_l < \varphi_{fr}$. Similarly, metastable crystallites of composition $\varphi_s < \varphi_m$ would melt for any size. If $\varphi_s > \varphi_m$ and $\varphi_l > \varphi_{fr}$, a crystallite would grow in a metastable liquid if its size were greater than R_{cr} but melt if it were smaller.

Figure 3 shows the composition at the solid-liquid interface, φ_{sR} and φ_{lR}, as a function of R and $J = 1 - e^F$ computed using the chemical potentials given by Eq. (1). Empty regions on the left-hand side of these diagrams represent the J, R values for which Eqs. (6) and (7) do not have a solution. A crystallite would grow if $J > 0$ ($F < 0$) and melt for $J < 0$ ($F > 0$). The radius of a stable ($J = F = 0$) crystallite is $R_{cr} = \Gamma/(\varphi_{sR_{cr}}\Delta\mu_{cr})$, where $\Delta\mu_{cr} = \mu_l(\varphi_{lR_{cr}}) - \mu_s(\varphi_{sR_{cr}})$ and $\Pi_s(\varphi_{sR_{cr}}) = \Pi_l(\varphi_{lR_{cr}}) + \Gamma/R_{cr}$. Consistent with results of the analysis presented above, a crystallite would remain stable in a metastable liquid, $\varphi_l (> \varphi_{fr})$, only if its size is R_{cr}; larger crystallites would grow but smaller melt. If $\varphi_l < \varphi_{fr}$, crystallites of any size would melt. Similarly, a crystallite, $\varphi_s (> \varphi_m)$,

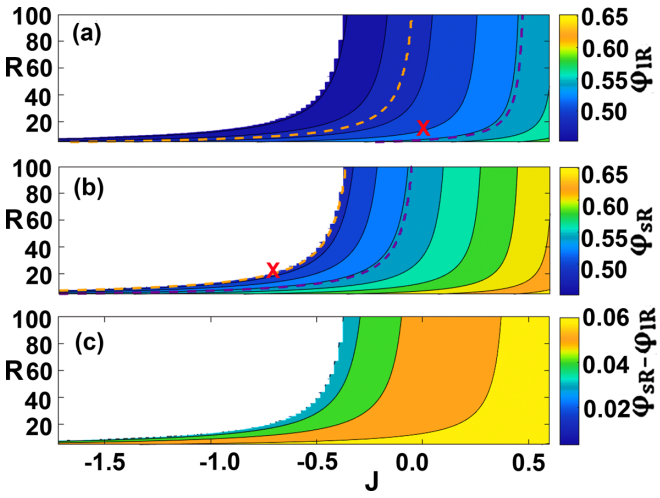

FIG. 3. Contour plots of constant volume fractions in (a) liquid phase φ_{lR}, (b) solid phase φ_{sR}, and (c) volume fraction jump $\varphi_{sR} - \varphi_{lR}$ vs $J = 1 - e^F$. Curves for the points φ_{fr} (dashed light) φ_m (dashed dark) are also plotted in panels (a) and (b). The cross in panel (a) shows the size of the critical nucleus measured in Ref. [41]. The cross in panel (b) shows the size of the smallest precritical nuclei measured in Ref. [42].

remains stable if its size is R_{cr}; larger crystallites would grow, but smaller melt. If $\varphi_s < \varphi_m$, metastable crystallites of any size would melt.

We note that direct imaging was used to study crystallization of suspensions of fluorescence spherical PMMA particles at single-particle resolution [41,42]. By measuring the time evolution of many crystallites, the authors of Ref. [41] plotted the difference between the probabilities with which crystallites grow or shrink as a function of the crystallite radius scaled by the particle radius for a suspension with the particle volume fraction of 0.47. This difference was found to vanish for the nucleus size of $R_{cr}/a \sim 6$. As it can be seen in Fig. 3(a), this point agrees well with the point at which $J = 0$ and $\varphi_{lR} = 0.47$. The authors of Ref. [42] imaged the birth, life, and death of a subcritical nucleus containing in a crystallizing colloid with the particle volume fraction of 0.51. The smallest precritical nuclei were observed to have a radius of $R/a \sim 20$. By measuring the interparticle spacing, they estimated the average particle volume fraction of precritical nuclei to be $\varphi_{sR} \sim 0.5$. The point representing the smallest precritical nuclei in Fig. 3(b) is close to the boundary of the empty region at $\varphi_{sR} \sim 0.5$. This is consistent with the fact that there are no precritical crystallites in the empty regions in Fig. 3. We point out that Eqs. (6) and (7) taken to compute diagrams in Fig. 3 do not include any fitting parameters.

B. Asymptotic model

The asymptotic analysis of the diffusion model is conducted for a sufficiently thin diffusion zone around a crystallite. The main emphasis is to consider the case when the particle diffusion coefficient in the liquid phase vanishes at a certain particle volume fraction φ_g. Note that this analysis does not assume the same particle diffusion coefficients in the solid and liquid phases. Moreover, the power-law

concentration dependence of the diffusion coefficient in the liquid phase given by Eq. (4) is only used to compare the asymptotic expressions with numerical simulations.

In the spirit of Ref. [27], the diffusion equations, Eqs. (2) and (3), can be approximated as quasisteady in a frame of reference moving with the interface $s = r - R(t)$:

$$v_R \frac{d\varphi_l}{ds} + \frac{d}{ds}\left[D_{c,l}(\varphi_l)\frac{d\varphi_l}{ds}\right] \approx 0 \text{ for } s > 0 \text{ with } \varphi_l|_{s=0} = \varphi_{lR},$$
$$v_R \frac{d\varphi_s}{ds} + \frac{d}{ds}\left[D_{c,s}(\varphi_s)\frac{d\varphi_s}{ds}\right] \approx 0 \text{ for } s < 0 \text{ with } \varphi_s|_{s=0} = \varphi_{sR}.$$

Integrating these equations and using Eq. (5) for the interfacial condition at $s = 0$, we find that the flux of particles j in this moving reference frame does not change across the solid-liquid interface:

$$j = v_R\varphi_l + D_{c,l}(\varphi_l)\frac{d\varphi_l}{ds} \quad \text{for } s > 0, \tag{9}$$

$$j = v_R\varphi_s + D_{c,s}(\varphi_s)\frac{d\varphi_s}{ds} \quad \text{for } s < 0. \tag{10}$$

Equation (9) shows that φ_l would monotonically increase or decrease from the value φ_{lR} across the diffusion zone in the liquid phase, depending on the sign of $j - v_R\varphi_l$. According to the boundary condition in Eq. (2), the particle diffusion flux in the liquid phase should vanish far away from the solid-liquid interface, $s \to \infty$. If $\varphi_{out} < \varphi_g$, $D_{c,l}(\varphi_l)$ does not vanish at φ_{out} [see Eq. (2)], so that this boundary condition requires $j = v_R\varphi_{out}$. However, if $\varphi_{out} > \varphi_g$, $D_{c,l}(\varphi_l)$ vanishes at $\varphi_l = \varphi_g$, and we then have $j = v_R\varphi_g$. Integration of Eq. (9) yields Eq. (11),

$$\int_{\varphi_{lR}}^{\varphi_l} \frac{D_{c,l}(\varphi_l)}{j - v_R\varphi_l} d\varphi_l = s \quad \text{with } j = v_R\varphi_{out} \text{ for } \varphi_{out} < \varphi_g \quad \text{and}$$
$$j = v_R\varphi_g \text{ for } \varphi_{out} > \varphi_g. \tag{11}$$

According to Eq. (10), φ_s would monotonically increase or decrease from the value φ_{sR}, depending on the sign of $j - v_R\varphi_s$. Therefore, the boundary condition in Eq. (3), that the diffusion flux in the solid phase should go to zero at $s \to -R(t)$, can be met only if $\varphi_s = \varphi_{sR}$ with $\varphi_{sR} = \varphi_{out}$ at $\varphi_{out} < \varphi_g$ and $\varphi_{sR} = \varphi_g$ at $\varphi_{out} > \varphi_g$. Equation (12) below summarizes this outcome:

$$\varphi_s = \varphi_{sR} \quad \text{with } \varphi_{sR} = \varphi_{out} \quad \text{for } \varphi_{out} < \varphi_g \quad \text{and}$$
$$\varphi_{sR} = \varphi_g \quad \text{at } \varphi_{out} > \varphi_g. \tag{12}$$

Taking φ_{sR} from Eq. (12), we can calculate φ_{lR} and v_R from Eqs. (6) and (7) for a given R. As Eq. (12) shows, the results strongly depend on whether φ_{out} is smaller or greater than φ_g, for which the particle long-time diffusivity in the liquid phase, Eq. (2), vanishes.

Numerical simulations presented below confirm that Eqs. (11) and (12) capture the asymptotic limit of relatively thin diffusion zones in the liquid and solid phases. As can be seen from Eqs. (11) and (12), cessation of long-time diffusivity above φ_g does not arrest the diffusion growth of a crystallite for $\varphi_{out} > \varphi_g$. We note that MD simulations [17] also show that hard-sphere colloids of very low polydispersity could crystallize well beyond φ_g.

Equations (11) and (12) demonstrate clearly that once a crystallite forms, its growth is then controlled by the particle diffusion in the depletion zone surrounding the crystallite, where φ_l is well below φ_g. We note again that this prediction is consistent with the appearance of a thin depletion zone surrounding a growing crystallite, first observed in Refs. [25,26] and later confirmed by other experiments reviewed in Refs. [1,4,5,27–30]. When $\varphi_{out} > \varphi_g$, Eqs. (11) and (12) define the finite thickness of the depletion zone for $\varphi_l \to \varphi_g$ as $\delta_g \approx \frac{1}{\zeta_L v_R}(\frac{d\mu_l}{d\varphi_l})_{\varphi_g}(1 - \varphi_{lR}/\varphi_g)^{\zeta_L}$, whereas $s \sim -D_{c,l}(\varphi_{out})\ln(\varphi_{out} - \varphi_l)/v_R \to \infty$ for $\varphi_l \to \varphi_{out} < \varphi_g$. Since φ_{sR} is known in both cases, the values of φ_{lR}, F, and v_R can then be calculated from Eq. (6) for a given R. For a sufficiently large crystallite radius, the asymptotic values $\varphi_{lR=\infty}$ and F_∞ from Eq. (8) for a flat solid-liquid interface (Fig. 2) can be taken in Eq. (7) for computing v_R. In this case, the crystallite growth rate is specified by the Wilson-Frenkel law for a flat solid-liquid interface and determined by the liquid composition φ_{out}.

Replacement of the diffusion coefficient $D_{c,l}(\varphi_l)$ in Eq. (11) with its average value provides an estimate for the thickness of the depletion zone:

$$\delta_{avg} = \frac{D_{c,l,avg}}{v_R} \quad \text{with} \quad D_{c,l,avg} = \frac{\int_{\varphi_{lR}}^{\varphi_*} D_{c,l}(\varphi_l)d\varphi_l}{\varphi_{out} - \varphi_{lR}}, \tag{13}$$

with $\varphi_* = \varphi_{out}$ or φ_g depending on the value φ_{out} and yields the following asymptotic expression for the particle distribution across the depletion zone:

$$\varphi_l = \varphi_{out} + (\varphi_{lR} - \varphi_{out})\exp\left(-\frac{r - R}{\delta_{avg}}\right) \quad \text{for } \varphi_{out} < \varphi_g. \tag{14}$$

For a sufficiently large crystallite radius, we can use the asymptotic value $\varphi_{lR=\infty}$ for φ_{lR} in Eq. (13) that is shown in Fig. 2. Neglecting the concentration dependence of $D_{c,l}(\varphi_l)$ in Eq. (14) yields the expression obtained in Ref. [27].

III. RESULTS AND DISCUSSION

We consider the growth of a crystallite formed in a metastable liquid-phase suspension within the fully crystalline state above the melting point. Simulations are conducted by taking the experimental data [22,43,44] listed in Table I: diffusion coefficient D_0, particle radius a, suspension volume fraction φ_{out}, and the initial crystallite size R and composition φ_{sR}. We use them to compute φ_{lR} from the pressure balance, Eq. (6), and estimate the initial thickness of the depletion zone, $\delta_0 = R_{out} - R$ from the mass balance $\varphi_{sR}R^3 + \varphi_{lR}(R_{out}^3 - R^3) = \varphi_{out}R_{out}^3$.

Plots in Fig. 4 shows variation of the volume fraction φ in the solid and liquid phases for a growing crystallite computed with the initial conditions from Table I, Ref. [22], for a suspension with $\varphi_{out} = 0.568$ that is slightly smaller than φ_g. Simulations presented in Fig. 4(a) are conducted using diffusion coefficients $D_{c,l}$ and $D_{c,s}$ given by Eq. (4) with $\alpha = 1$ and $m = M_s$ in the expression for v_∞ in Eq. (7). These plots show that the depletion zone in the liquid phase exhibits a sharp transition of φ to φ_{out}. In the central part of the crystallite, $r \leqslant R$, φ remains at the initial value as Eq. (2) yields zero for the particle diffusivity. Plots in Fig. 4(b) illustrate the importance of including concentration dependence of the diffusion coefficients given by Eq. (4). They are obtained using the same

TABLE I. Data from experiments in Refs. [22,43,44]; suspension composition φ_{out}, particle radius a, Stokes-Einstein diffusion coefficient D_0, $\tau = a^2/D_0$, L and φ_{sR} are the size and composition of crystallites formed at the early stage of crystallization, nondimensional crystallite radius $R = L/2a$, the liquid composition φ_{lR} computed from Eq. (6) for those φ_{sR} and R, and the radius of depletion zone R_{out} computed from the particle balance.

φ_{out}	a, nm	D_0, $\mu m^2/s$	$L/2$, μm	φ_{sR}	τ, s	R	φ_{lR}	R_{out}	Ref.
0.552	300	0.37	4.14	0.569	0.243	13.8	0.511	15.5	[43]
0.553	200	0.85	3.58	0.611	0.047	17.9	0.549	44.6	[44]
0.557			3.72	0.611		18.6	0.549	36.8	
0.561			3.70	0.620		18.5	0.558	50.8	
0.565			3.90	0.623		19.5	0.561	48.6	
0.559	424	0.17	7.84	0.581	1.058	18.5	0.521	21.5	[22]
0.568			7.17	0.607		16.9	0.545	23.5	

initial conditions as in Fig. 4(a) but with $D_{c,l} = D_{c,s} = 1$. Compared to Fig. 4(a), it yields a much wider depletion zone in the liquid phase, a smooth transition of the particle volume fraction to φ_{out}, and a gradually decreasing particle volume fraction in the crystallite due to nonvanishing diffusivity. Plots in Fig. 4(c) show that with increasing time φ_{sR}, φ_{lR}, dR/dt, and accordingly the log-log plot of R(t) approach their asymptotic values given by Eqs. (11) and (12).

Plots in Fig. 5 show the variation of the volume fraction φ in the liquid phase ($r > R$) computed with the initial conditions from Table I, Refs. [22] and [43]. Simulations are conducted with diffusion coefficients $D_{c,l}$ and $D_{c,s}$ given by Eq. (4). The length across the depletion zone is expressed in units of δ_{avg} calculated from Eq. (13) using simulation results. Plots in Fig. 5(a) demonstrate that decreasing φ_{out} leads to a smoother transition between the depletion zone and the far-field volume fraction. Plots in Fig. 5(b) show that expressions (11) and (12) capture well the particle distribution in the liquid phase. However, Eq. (14) that neglects the concentration dependence of $D_{c,l}$ gives very different results. Instead of providing a compact, well-defined depletion zone with φ transitioning abruptly to φ_{out}, it yields an extended depletion zone with φ approaching φ_{out} asymptotically. It therefore cannot be used to estimate the onset of ripening.

Simulations reveal that the strong concentration dependence of the particle transport defined by Eq. (4) is a crucial factor governing the crystallite growth. Specifically, the depletion zone in the liquid phase remains thin and is characterized by a sharp transition of φ_l to φ_{out}. This prediction is consistent with experiments on shear-melted suspensions with $\varphi_{out} > \varphi_m$, whereas a depletion zone growing approximately as $\sqrt{t}$ was observed for $\varphi_{out} < \varphi_m$ [30]. It is also found that φ_{sR} and φ_{lR} defined by Eqs. (6) and (7) gradually decrease with time as was observed in Refs. [23,43,44] for suspensions characterized by $\varphi_{out} > \varphi_m$.

Simulations show that the crystallite growth rate rises gradually to a plateau value which represents the asymptotic limit of relatively thin diffusion zones in the liquid and solid phases near the solid-liquid interface when $D_{c,l}/v_R \ll R$ and $D_{c,s}/v_R \ll R$.

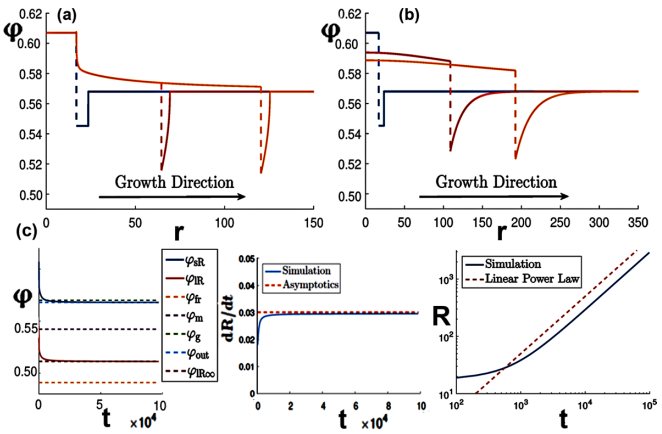

FIG. 4. (a), (b): Volume fraction φ in solid and liquid phases. Crystallite forms at t = 0 (blue) and grows to the right, t = 2000 (red) and 4000 (yellow); initial conditions from Table I, Ref. [22],: $\varphi_{out} = 0.568$, $R = 16.9$, $\varphi_{sR} = 0.607$, $\varphi_{lR} = 0.545$, $R_{out} = 23.5$, $\alpha = 1$, and $m = M_s$ in the expression for v_∞ in Eq. (7). Dashed lines show positions of the solid-liquid interface. (a) $D_{c,l}$ and $D_{c,s}$ given by Eq. (4). (b) $D_{c,l} = D_{c,s} = 1$. (c) $D_{c,l}$ and $D_{c,s}$ given by Eq. (4). Time variation of φ_{sR} (top solid curve), φ_{lR} (bottom solid curve); dR/dt, R; dashed lines show asymptotic predictions.

A. Solid-liquid interface mobility

We use simulations to evaluate v_∞ in the Wilson-Frenkel law from the experimental data obtained in terrestrial [22,44,45] and microgravity [43] experiments on

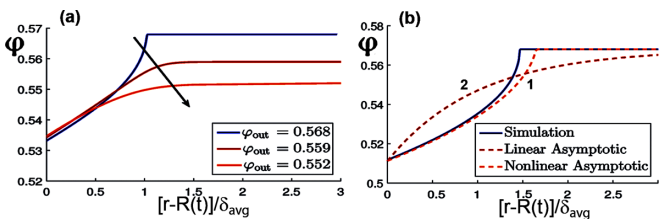

FIG. 5. Simulations with $D_{c,l}$ and $D_{c,s}$ given by Eq. (4). Variation of volume fraction φ in the liquid phase ($r > R$) computed for the initial conditions from Table I, Refs. [22] and [43]: $\varphi_{out} = 0.568$, $R = 16.9$, $\varphi_{sR} = 0.607$, $\varphi_{lR} = 0.545$, $R_{out} = 23.5$; $\varphi_{out} = 0.559$, $R = 18.5$, $\varphi_{sR} = 0.581$, $\varphi_{lR} = 0.521$, $R_{out} = 21.5$; $\varphi_{out} = 0.552$, $R = 13.8$, $\varphi_{sR} = 0.569$, $\varphi_{lR} = 0.511$, and $R_{out} = 15.5$. Curves are plotted at t = 105; δ_{avg} is the scale along the horizontal axis calculated from Eq. (13) from simulation results. (a) Arrow shows decreasing volume fractions φ_{out}. (b) Numerical simulations (solid blue curve), asymptotic predictions by Eqs. (11) and (12) (dashed curve 1) and Eq. (14) (dashed curve 2).

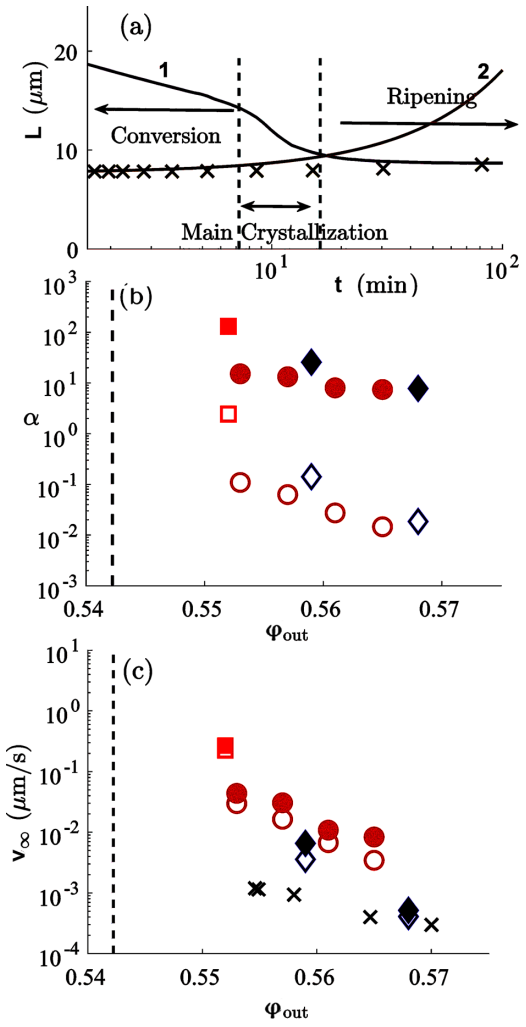

FIG. 6. Computation of solid-liquid interface mobility in the Wilson-Frenkel law from experiments. (a) Curve 1 and crosses show L_c and crystallize sizes from Ref. [44] for $\varphi_{out} = 0.565$; curve 2 shows crystallize growth computed with fitted α for m equal to M_s; (b) α computed by taking M_s (hollow symbols) and M_L (solid symbols) for m; diamonds [22], circles [44], squares [43]. (c) v_∞ computed for both options; crosses shows measurements in Ref. [45].

crystallization of metastable suspensions for φ_{out} within the range $[\varphi_m, \varphi_g]$ (Fig. 6). Unfortunately, crystallization kinetics for $\varphi_{out} > \varphi_g$ in microgravity was not recorded [10,11]. In experiments [22,43–45], the ripening stage of crystallization started much earlier compared to the crystallite growth entering the constant velocity regime given by asymptotic equations (11) and (12). As our model considers the growth of a single crystallite, we use it only over a limited period of time, t_i, from the early stage of crystallization, set as $t = 0$ in simulations, up to the onset of ripening in an experiment. Specifically, we consider that the crystallite diameter 2aR computed at this instance becomes equal to the separation between centers of neighboring crystallites $L_c = 1/N_c^{1/3}$, where N_c is the measured number density of crystallites $2aR(t_i) = 1/[N_c(t_i)]^{1/3}$. The calculated value of t_i decreases monotonically with increasing α. We use it as a self-consistent way to tune α by requiring t_i be equal to the onset of ripening in an experiment. Initial conditions for these simulations are taken from data [22,43,44] in Table I. We note that this approach ignores the presence of a depletion zone surrounding a crystallite. To estimate its influence, the computed crystallite size was augmented by the thickness of the depletion zone. As the depletion zone sharpness reduces with decreasing φ_{out}, we define it as the region where a difference between the local volume fraction and φ_{out} is greater than 4%. Adding the depletion zone thickness is found to change α by about 5%. The contribution of changing the criterion for finding the depletion zone thickness is of a similar order. We note that the instants at which the crystallization and ripening stages started are given explicitly only in Ref. [22]; for other experiments we estimate them in the manner consistent with [22].

As an example, plots in Fig. 6(a) show data on L_c and crystallite sizes from Ref. [44] and the crystallite growth computed for the fitted α. Figure 6(b) presents α found with the use of M_L and M_s for m in the expression for v_∞ in Eq. (7). While there appears to be a nearly constant offset between the values of α obtained for M_L and M_s, the values of v_∞ computed using either option for m nearly overlap in Fig. 6(c). This overlap of data on v_∞, recalling that α in Fig. 6(b) varies substantially with the suspension volume fraction, does not support the hypothesis [3–5,27–29] for strong correlation between v_∞ and either the particle long- or short-time diffusivity in the bulk suspension. In contrast, it indicates that the particle mobility in the transition region between the solid and liquid phases is substantially greater than its long-term mobility in the bulk liquid, but substantially lower than its short-time mobility.

The computed values of v_∞ presented in Fig. 6(c) are consistent with direct measurements of v_∞ in Ref. [45]. Taking experimental data [46] on colloidal crystallization assisted by an electric field, we estimate $v_\infty \sim 0.1\mu$m/s at $\varphi_{out} = 0.145$ that lies within the range of data in Fig. 6(c). The largest value for v_∞ in Fig. 6(c) is found in microgravity [43]. However, its deviation compares to the differences between the data computed for terrestrial experiments [22,44,45].

We note that the range of values of v_∞ presented in Fig. 6(c) is by several orders of magnitude smaller than the range of data for the speed of diffusionless crystal growth in charged colloidal systems measured under deep supercooling [19]. Experimental data [18,19] and results of MD simulations for hard-sphere [17], soft [18], and charged [19] colloidal suspensions demonstrate that the fast diffusionless crystallization of dense colloids is associated with cooperative displacements of colloidal particles, each less than a particle diameter, and that it proceeds without the macroscopic particle diffusion in the noncrystalline phase. In contrast, the range of values of v_∞ seen in Fig. 6(c) is consistent with the diffusion mechanism for the crystallite growth considered in the proposed model; see Eqs. (2)–(7).

B. Gravity effect

We now summarize what is known about the gravity influence on colloidal crystallization. Colloids with the volume fraction greater than $\varphi_g \sim 0.57-0.58$ crystalize in microgravity [10,11], but not on the Earth [3–7]. Nevertheless, there

is no drastic difference between the data in Fig. 6(c) on the solid-liquid interface mobility in microgravity and terrestrial experiments. Next, terrestrial experiments [20,23,24] reveal a similarity in the behavior of low-symmetry crystal precursors which form in shear-melted suspensions at particle volume factions below and above φ_g, but do not grow if the volume fraction is larger than φ_g. We demonstrate that cessation of the particle long-time diffusivity above φ_g does not arrest the crystallite growth. By taking all these findings together, it is tempting to speculate that gravitational sedimentation of particles within the diffusion zone around a crystallite hinders its growth in colloids with the volume fraction greater than $0.57-0.58$. However, the important question of what precise mechanism gravity affects particle movements requires further investigation.

IV. CONCLUSIONS

We consider the initial stage of crystallization of dense hard-sphere colloids in a setup such that diffusion zones around different crystallites do not overlap, and each crystallite grows independently. We use the classical model for the crystallite growth that combines diffusion equations for the particle transport in the liquid and solid phases, coupled with the particle flux balance and thermodynamic relations at the crystallite surface. The Wilson-Frenkel law is used to compute the motion of the solid-liquid interface. The crucial feature of our formulation is that we include the facts that (i) increasing the volume fraction reduces and eventually arrests the particle diffusion, and (ii) the composition of a growing crystallite changes with size. Previous approaches sidestepped these major features of colloids.

Numerical simulations are used to evaluate the velocity of the solid-liquid interface from the data obtained in terrestrial and microgravity experiments on crystallization of metastable suspensions. The reported estimates demonstrate that the mobility of colloidal particles in the transition region between the solid and liquid phases is substantially larger than the long-term mobility in the bulk liquid, but substantially lower than the short-time mobility. This range of data for the solid-liquid interface velocity is consistent with the diffusion mechanism for the crystallite growth considered in our model. The presented results suggest that cessation of the particle long-time diffusion above certain volume fraction does not suppress the crystallite growth in hard-sphere colloids. Once a crystallite forms, its growth is then controlled by the particle diffusion in the depletion zone surrounding the crystallite.

We also demonstrate that there is no drastic difference between the data on the solid-liquid interface mobility in microgravity and on Earth. It is conceivable that even a very slow gravitational sedimentation of particles in dense colloids can arrest colloidal crystallization by redirecting the particle transport. The insight into the effect of vanishing particle mobility and particle sedimentation on crystallization of colloids will help engineer colloidal materials with controllable structure.

ACKNOWLEDGMENTS

We are thankful to Thomas Palberg, Johannes Gutenberg-Universität, Mainz and Paul Chaikin, New York University for very helpful conversations and valuable comments on the earlier version of the paper. The work was supported in part by NASA Grant No. NNX16AQ79G, NSF Grant No. CBET-1832260, and Glenn Engineering and Research Support Contract No. 80GRC020D0003.

B.K., L.K. and W.V.M. conceptualized the work; B.K. conducted asymptotic analysis; M.A.L. carried out numerical simulations.

APPENDIX: NUMERICAL METHOD

A conservative finite-volume method with an adaptive mesh is used to solve Eqs. (2) and (3) with the boundary conditions Eqs. (5)–(7) at the moving solid-liquid interface. We form a nonequispaced partition of $N+1$ points denoted by r_i, $i = 0, 1, \ldots, N$ with the point M^j at the moving solid-liquid interface at the instant t^j such that $r_{M^j} = R^j \equiv R(t^j)$. The cell average volume fraction $\bar{\varphi}_i$ and the flux $Q_i = [r^2 D_c(\varphi)\partial\varphi/\partial r]_i$ in the grid point r_i are defined as

$$\bar{\varphi}_i = \frac{1}{V_i}\int_{r_i}^{r_{i+1}} r^2\varphi dr \quad \text{with} \quad V_i = \frac{r_{i+1}^3 - r_i^3}{3} \quad \text{and} \quad \bar{\varphi}_i(t) = \varphi(r_{i+1/2}, t) + O(\Delta r^2) \quad \text{with} \quad r_{i+1/2} = \frac{r_{i+1} + r_i}{2}$$

$$Q_i = r_i^2\left[\frac{r_{i+1/2} - r_i}{r_{i+1/2} - r_{i-1/2}} D_c(\bar{\varphi}_i) + \frac{r_i - r_{i-1/2}}{r_{i+1/2} - r_{i-1/2}} D_c(\bar{\varphi}_{i-1})\right]\frac{\bar{\varphi}_i - \bar{\varphi}_{i-1}}{r_{i+1/2} - r_{i-1/2}} + O(\Delta r^2),$$

where φ_i, D_c are either φ_{li}, $D_{c,l}$ or φ_{si}, $D_{c,s}$, depending on the suspension phase where the point r_i is evaluated. With these expressions, the diffusion equations (2) and (3) away from the points r_{M^j} and r_{M^j-1} can be presented as

$$\frac{\partial\bar{\varphi}_i}{\partial t} = \frac{f_i}{V_i} \quad \text{with} \quad f_i = Q_{i+1} - Q_i \quad \text{for} \quad 0 \leqslant i \leqslant M^j - 2 \;\&\; M^j + 1 \leqslant i \leqslant N - 1 \quad \text{and} \quad Q_0 = Q_N \equiv 0.$$

For points $i = M^j - 1$ and $i = M^j$, expressions Eqs. (2), (3), and (5) are combined to yield

$$V_{M^j-1}\frac{\partial\bar{\varphi}_{M^j-1}}{\partial t} + V_{M^j}\frac{\partial\bar{\varphi}_{M^j}}{\partial t} = Q_{M^j+1} - Q_{M^j-1} + (\varphi_{lR} - \varphi_{sR})r_{M^j}^2 v_R(\varphi_{sR}, \varphi_{lR}) + O(\Delta r^2),$$

where the volume fractions, φ_{sR} and φ_{lR}, in this expression, as well as in Eqs. (6) and (7) at the moving solid-liquid interface, $r_{M^j} = R^j$, are expressed in terms of $\bar{\varphi}_{M^j-1}$ and $\bar{\varphi}_{M^j}$ as

$$\varphi_{sR} = \frac{r_{M^j} - r_{M^j-3/2}}{r_{M^j-1/2} - r_{M^j-3/2}}\bar{\varphi}_{M^j-1} + \frac{r_{M^j-1/2} - r_{M^j}}{r_{M^j-1/2} - r_{M^j-3/2}}\bar{\varphi}_{M^j-2} + O(\Delta r^2),$$

$$\varphi_{lR} = \frac{r_{M^j+3/2} - r_{M^j}}{r_{M^j+3/2} - r_{M^j+1/2}}\bar{\varphi}_{M^j} + \frac{r_{M^j} - r_{M^j+1/2}}{r_{M^j+3/2} - r_{M^j+1/2}}\bar{\varphi}_{M^j+1} + O(\Delta r^2)$$

$$\Pi_s\left(\frac{r_{M^j} - r_{M^j-3/2}}{r_{M^j-1/2} - r_{M^j-3/2}}\bar{\varphi}_{M^j-1} + \frac{r_{M^j-1/2} - r_{M^j}}{r_{M^j-1/2} - r_{M^j-3/2}}\bar{\varphi}_{M^j-2}\right)$$
$$= \Pi_l\left(\frac{r_{M^j+3/2} - r_{M^j}}{r_{M^j+3/2} - r_{M^j+1/2}}\bar{\varphi}_{M^j} + \frac{r_{M^j} - r_{M^j+1/2}}{r_{M^j+3/2} - r_{M^j+1/2}}\bar{\varphi}_{M^j+1}\right) + \frac{\Gamma}{R^j} + O(\Delta r^2).$$

We apply three conditions to determine when to refine the grid by adding a point or to coarsen it by removing a point. First, we enforce a maximum spatial step size, $\Delta r_{MAX}(r)$, which linearly scales between some minimum step size near the interface, Δr_{min}, and some maximum step size, Δr_{max}, far away from the interface as $\Delta r_{MAX}(r) = \Delta r_{max}$ at $|r - R^j| > \delta_{avg}$ and $\Delta r_{MAX}(r) = \Delta r_{min} + (\Delta r_{max} - \Delta r_{min})|r - R^j|/\delta_{avg}$ at $|r - R^j| < \delta_{avg}$. Secondly, it depends on the relative variation of the volume fraction from point to point that is characterized by the following parameters:

$$\epsilon_{chg}(i) = \frac{|\bar{\varphi}_{i+1} - \bar{\varphi}_i|}{\bar{\varphi}_{i+1} - \bar{\varphi}_i} \quad \text{and} \quad \epsilon_{curv}(i) = \frac{\Delta r_i}{\rho_i} \quad \text{with} \quad \rho_i = \left.\frac{(1 + \partial\varphi/\partial r)^{3/2}}{|\partial^2\varphi/\partial r^2|}\right|_{r=r_i},$$

where ρ_i is the local curvature of the function φ vs r evaluated with a second-order accurate finite-difference scheme; $\epsilon_{curv}(i)$ for small Δr_i is equal to the sagitta of a circular arc of length Δr_i that is, the distance from the center of the arc to the center of its base. Numerical tests show that the adaptive scheme performs best when a new point is added at the midpoint between points r_i and r_{i+1} if $\epsilon_{curv}(i) > \Delta r_{min}$ or $\epsilon_{chg}(i) > \Delta r_i$, and the point r_i is removed if $\epsilon_{curv}(i) < 0.1\Delta r_{min}$ or $\epsilon_{chg}(i) < \Delta r_i^2$. Points are added or removed such that $\Delta r_{min} < \Delta r_i < \Delta r_{MAX}(r_i)$.

When a point is added or removed, nearby values of volume fractions on the adjusted grid are calculated to maintain the local mass balance. If a removed point r_i is not adjacent to the interface, we set $\widetilde{\bar{\varphi}}_{i-1} = (\bar{\varphi}_{i-1}V_{i-1} + \bar{\varphi}_i V_i)/\tilde{V}_{i-1}$, where tilde denotes values on the adjusted grid. When a point $\tilde{r}_{i+1} = (r_i + r_{i+1})/2$ is added between r_i and r_{i+1} so that r_i and r_{i+1} become, respectively, $\tilde{r}_i$ and $\tilde{r}_{i+2}$, we set $\widetilde{\bar{\varphi}}_i = \widetilde{\bar{\varphi}}_{i+1} = \bar{\varphi}_i$ and $\widetilde{\bar{\varphi}}_{i+2} = \bar{\varphi}_{i+1}$ with the accuracy of $O(\Delta r^2)$. When a new point is added near the solid-liquid interface in the solid phase at $\tilde{r}_{M-1} = (r_{M-1} + r_M)/2$ or the liquid phase at $\tilde{r}_{M+1} = (r_M + r_{M+1})/2$, volume fractions at this and next adjacent points on the adjusted grid, $\widetilde{\bar{\varphi}}_{M-1}$, $\widetilde{\bar{\varphi}}_{M-2}$ or $\widetilde{\bar{\varphi}}_M$, $\widetilde{\bar{\varphi}}_{M+1}$, are calculated to maintain the interface volume fraction, $\varphi_{sR} = \bar{\varphi}_{sR}$ or $\varphi_{lR} = \bar{\varphi}_{lR}$, and the local mass balance $\bar{\varphi}_{M-1}V_{M-1}$ between r_{M-1} and r_M or $\bar{\varphi}_M V_M$ between r_M and r_{M+1}, respectively. The same requirements are applied when a point near the solid-liquid interface is removed in the solid or liquid phase.

The following finite-difference scheme is developed to evolve the solution from time step t^j to time step $t^{j+1} = t^j + \Delta t$. First, the forward Euler method is used to calculate R^{j+1} and $\bar{\varphi}_i^{j+1}$ for $1 \leqslant i \leqslant M^j - 2$ & $M^j + 1 \leqslant i \leqslant N - 1$:

$$R^{j+1} = R^j + \Delta t v_R(\varphi_{sR}^j, \varphi_{lR}^j) \quad \text{and} \quad \bar{\varphi}_i^{j+1} = \bar{\varphi}_i^j + \Delta t\frac{f_i^j}{V_i}.$$

We then use the Newton-Raphson iterative method to compute $\bar{\varphi}_{M^j-1}^{j+1}$ and $\bar{\varphi}_{M^j}^{j+1}$ from two coupled equations,

$$V_{M^j-1}(\bar{\varphi}_{M^j-1}^{j+1} - \bar{\varphi}_{M^j-1}^j) + V_{M^j}(\bar{\varphi}_{M^j}^{j+1} - \bar{\varphi}_{M^j}^j) = \Delta t\left[Q_{M^j+1}^j - Q_{M^j-1}^j + (\varphi_{lR}^j - \varphi_{sR}^j)r_{M^j}^2 v_R(\varphi_{sR}^j, \varphi_{lR}^j)\right],$$

$$\Pi_s\left(\frac{r_{M^j} - r_{M^j-3/2}}{r_{M^j-1/2} - r_{M^j-3/2}}\bar{\varphi}_{M^j-1}^{j+1} + \frac{r_{M^j-1/2} - r_{M^j}}{r_{M^j-1/2} - r_{M^j-3/2}}\bar{\varphi}_{M^j-2}^{j+1}\right) = \Pi_l\left(\frac{r_{M^j+3/2} - r_{M^j}}{r_{M^j+3/2} - r_{M^j+1/2}}\bar{\varphi}_{M^j}^{j+1} + \frac{r_{M^j} - r_{M^j+1/2}}{r_{M^j+3/2} - r_{M^j+1/2}}\bar{\varphi}_{M^j+1}^{j+1}\right) + \frac{\Gamma}{R^{j+1}},$$

We note that a much smaller time step is required during the early times of the numerical scheme ($t < 40$) than that estimated from the Courant-Friedrichs-Lewy stability condition $v_R\Delta t/\Delta r_{min} \sim 1$. It is needed to suppress oscillations in the volume fractions at the solid-liquid interface in early times. We therefore initially use an equipartitioned grid with grid spacing Δr_{min} with Δt being 128th of the value given by this condition. For $t > 40$, we begin applying the additive mesh procedure and relax Δt back to the estimated value.

[1] A. P. Gast and W. B. Russel, Simple ordering in complex fluids, Phys. Today **51**(12), 24 (1998).

[2] V. N. Manoharan, Colloidal matter: Packing, geometry, and entropy, Science **349**, 1253751 (2015).

[3] T. Palberg, Crystallization kinetics of repulsive colloidal spheres, J. Phys.: Condens. Matter **11**, R323 (1999).
[4] T. Palberg, Crystallization kinetics of colloidal model suspensions: Recent achievements and new perspectives, J. Phys: Condens. Matter **26**, 333101 (2014).
[5] D. M. Herlach, T. Palberg, I. Klassen, S. Klein, and R. Kobold, Overview: Experimental studies of crystal nucleation: Metals and colloids, J. Chem. Phys. **145**, 211703 (2016).
[6] P. N. Pusey and W. van Megen, Phase behaviour of concentrated suspensions of nearly hard colloidal spheres, Nature (London) **320**, 340 (1986).
[7] P. N. Pusey and W. van Megen, Observation of a Glass Transition in Suspensions of Spherical Colloidal Particles, Phys. Rev. Lett. **59**, 2083 (1987).
[8] M. D. Rintoul and S. Torquato, Metastability and Crystallization in Hard-Sphere Systems, Phys. Rev. Lett. **77**, 4198 (1996).
[9] I. Volkov, M. Cieplak, J. Koplik, and J. R. Banavar, Molecular dynamics simulations of crystallization of hard spheres, Phys. Rev. E **66**, 061401 (2002).
[10] J. Zhu, M. Li, R. Rogers, W. V. Meyer, R. H. Ottewill, STS-73 Space Shuttle Crew, W. B. Russel and P. M. Chaikin, Crystallization of hard-sphere colloids in microgravity, Nature (London) **387**, 883 (1997).
[11] Z. Cheng, P. M. Chaikin, W. B. Russel, W. V. Meyer, J. Zhu, R. B. Rogers, and R. H. Ottewill, Phase diagram of hard spheres, Mater. Design **22**, 529 (2001).
[12] W. van Megen, V. A. Martinez, and G. Bryant, Arrest of Flow and Emergence of Activated Processes at the Glass Transition of a Suspension of Particles with Hard Sphere Like Interactions, Phys. Rev. Lett. **102**, 168301 (2009).
[13] M. Hermes and M. Dijkstra, Thermodynamic signature of the dynamic glass transition in hard spheres, J. Phys: Condens. Matter **22**, 104114 (2010).
[14] E. Sanz, C. Valeriani, E. Zaccarelli, W. C. K. Poon, P. N. Pusey, and M. E. Cates, Crystallization Mechanism of Hard Sphere Glasses, Phys. Rev. Lett. **106**, 215701 (2011).
[15] G. L. Hunter and E. R. Weeks, The physics of the colloidal glass transition, Rep. Prog. Phys. **75**, 066501 (2012).
[16] J. F. Robinson, F. Turci, R. Roth, and C. P. Royall, Morphometric Approach to Many-Body Correlations in Hard Spheres, Phys. Rev. Lett. **122**, 068004 (2019).
[17] E. Zaccarelli, C. Valeriani, E. Sanz, W. C. K. Poon, M. E. Cates, and P. N. Pusey, Crystallization of Hard-Sphere Glasses, Phys. Rev. Lett. **103**, 135704 (2009).
[18] D. Ganapathi, D. Chakrabarti, A. K. Sood, and R. Ganapathy, Structure determines where crystallization occurs in a soft colloidal glass, Nat. Phys. **17**, 114 (2021).
[19] Q. Gao, J. Ai, S. Tang, M. Li, Y. Chen, J. Huang, H. Tong, L. Xu, L. Xu, H. Tanaka, and P. Tan, Fast crystal growth at ultralow temperatures, Nat. Mater. **20**, 1431 (2021).
[20] E. R. Weeks, J. C. Crocker, A. C. Levitt, A. Schofield, and D. A. Weitz, Three-dimensional direct imaging of structural relaxation near the colloidal glass transition, Science **287**, 627 (2000).
[21] H. J. Schöpe, G. Bryant, and W. van Megen, Two-Step Crystallization Kinetics in Colloidal Hard-Sphere Systems, Phys. Rev. Lett. **96**, 175701 (2006).
[22] S. Iacopini, T. Palberg, and H. J. Schöpe, Crystallization kinetics of polydisperse hard-sphere-like microgel colloids: Ripening dominated crystal growth above melting, J. Chem. Phys. **130**, 084502 (2009).
[23] M. Franke, S. Golde, and H. J. Schöpe, Solidification of a colloidal hard sphere like model system approaching and crossing the glass transition, Soft Matter **10**, 5380 (2014).
[24] S. Golde, T. Palberg, and H. J. Schöpe, Correlation between dynamical and structural heterogeneities in colloidal hard-sphere suspension, Nat. Phys. **12**, 712 (2016).
[25] D. J. W. Aastuen, N. A. Clark, L. K. Cotter, and B. J. Ackerson, Nucleation and Growth of Colloidal Crystals, Phys. Rev. Lett. **57**, 1733 (1986).
[26] K. Schätzel and B. J. Ackerson, Observation of Density Fluctuations During Crystallization, Phys. Rev. Lett. **68**, 337 (1992).
[27] W. B. Russel, P. M. Chaikin, J. Zhu, W. V. Meyer, and R. Rogers, Dendritic growth of hard sphere crystals, Langmuir **13**, 3871 (1997).
[28] B. J. Ackerson and K. Schätzel, Classical growth of hard-sphere colloidal crystals, Phys. Rev. E **52**, 6448 (1995).
[29] S. Derber, T. Palberg, K. Schätzel, and J. Vogel, Growth of a colloidal crystallite of hard spheres, Physica A **235**, 204 (1997).
[30] R. Beyer, M. Franke, H. J. Schöpe, E. Bartsch, and T. Palberg, From nuclei to micro-structure in colloidal crystallization: Investigating intermediate length scales by small angle laser light scattering, J. Chem. Phys. **143**, 064903 (2015).
[31] R. J. Speedy, Pressure of the metastable hard-sphere fluid, J. Phys.: Condens. Matter **9**, 8591 (1997).
[32] R. J. Speedy, Pressure and entropy of hard-sphere crystals, J. Phys.: Condens. Matter **10**, 4387 (1998).
[33] T. Zykova-Timan, J. Horbach, and K. Binder, Monte Carlo simulations of the solid-liquid transition in hard spheres and colloid-polymer mixtures, J. Chem. Phys. **133**, 014705 (2010).
[34] H. W. Wilson, On the velocity of solidification and viscosity of super-cooled liquids, London Edinburgh Philos. Mag. J. Sci. **50**, 238 (1900).
[35] J. Frenkel, Note on the relation between the speed of crystallization and viscosity, Phys. Z. Sowjetunion **1**, 498 (1932).
[36] H. M. Vollebregt, R. G. M. van der Sman, and R. M. Boom, Suspension flow modelling in particle migration and microfiltration, Soft Matter **6**, 6052 (2010).
[37] W. van Megen, T. C. Mortensen, S. R. Williams, and J. Müller, Measurement of the self-intermediate scattering function of suspensions of hard spherical particles near the glass transition, Phys. Rev. E **58**, 6073 (1998).
[38] W. van Megen, T. C. Mortensen, and G. Bryant, Change in relaxation scenario at the order-disorder transition of a colloidal fluid of hard spheres seen from the Gaussian limit of the self-intermediate scattering function, Phys. Rev. E **72**, 031402 (2005).
[39] H. Löwen, T. Palberg, and R. Simon, Dynamical Criterion for Freezing of Colloidal Liquids, Phys. Rev. Lett. **70**, 1557 (1993).
[40] F. Bitzer, T. Palberg, H. Löwen, R. Simon, and P. Leiderer, Dynamical test of interaction potentials for colloidal suspensions, Phys. Rev. E **50**, 2821 (1994).
[41] U. Gasser, E. R. Weeks, A. Schofield, P. N. Pusey, and D. A. Weitz, Real-space imaging of nucleation and growth in colloidal crystallization, Science **292**, 258 (2001).
[42] M. S. Elliot, S. B. Haddon, and W. C. K. Poon, Direct observation of pre-critical nuclei in a metastable

hard-sphere fluid, J. Phys.: Condens. Matter **13**, L553 (2001)

[43] Z. Cheng, J. Zhu, W. B. Russel, W. V. Meyer, and P. M. Chaikin, Colloidal hard-sphere crystallization kinetics in microgravity and normal gravity, Appl. Opt. **40**, 4146 (2001).

[44] J. L. Harland and W. van Megen, Crystallization kinetics of suspensions of hard colloidal spheres, Phys. Rev. E **55**, 3054 (1997).

[45] C. Sinn, A. Heymann, A. Stipp, and T. Palberg, Solidification kinetics of hard-sphere colloidal suspensions, in *Trends in Colloid and Interface Science XV. Progress in Colloid and Polymer Science*, edited by P. G. Koutsoukos (Springer, Berlin, Heidelberg, 2001), Vol. 118, pp. 266–275.

[46] H. Hwang, D. A. Weitz, and F. Spaepen, Direct observation of crystallization and melting with colloids, Proc. Natl. Acad. Sci. USA **116**, 1180 (2019).